Atmos. Chem. Phys. Discuss., 15, 16615–16654, 2015
www.atmos-chem-phys-discuss.net/15/16615/2015/
doi:10.5194/acpd-15-16615-2015


Atmospheric Chemistry and Physics Discussions
Open Access



# An online aerosol retrieval algorithm using OMI near-UV observations based on the optimal estimation method

**U. Jeong[1], J. Kim[1], C. Ahn[2], O. Torres[3], X. Liu[5], P. K. Bhartia[3], R. J. D. Spurr[4], D. Haffner[3], K. Chance[5], and B. N. Holben[3]**

[1]Dept. of Atmospheric Sciences, Yonsei University, Seoul, Korea
[2]Science Systems and Applications, Inc., Lanham, Maryland, USA
[3]Goddard Space Flight Center, NASA, Greenbelt, Maryland, USA
[4]RT Solutions, Inc., 9 Channing Street, Cambridge, Massachusetts, USA
[5]Harvard-Smithsonian Center for Astrophysics, Cambridge, Massachusetts, USA

Received: 26 March 2015 – Accepted: 19 May 2015 – Published: 18 June 2015

Correspondence to: J. Kim (jkim2@yonsei.ac.kr)

Published by Copernicus Publications on behalf of the European Geosciences Union.

## Abstract

An online version of the OMI (Ozone Monitoring Instrument) near-ultraviolet (UV) aerosol retrieval algorithm was developed to retrieve aerosol optical thickness (AOT) and single scattering albedo (SSA) based on the optimal estimation (OE) method. Instead of using the traditional look-up tables for radiative transfer calculations, it performs online radiative transfer calculations with the Vector Linearized Discrete Ordinate Radiative Transfer (VLIDORT) model to eliminate interpolation errors and improve stability. The OE-based algorithm has the merit of providing useful estimates of uncertainties simultaneously with the inversion products. The measurements and inversion products of the Distributed Regional Aerosol Gridded Observation Network campaign in Northeast Asia (DRAGON NE-Asia 2012) were used to validate the retrieved AOT and SSA. The retrieved AOT and SSA at 388 nm have a correlation with the Aerosol Robotic Network (AERONET) products that is comparable to or better than the correlation with the operational product during the campaign. The estimated retrieval noise and smoothing error perform well in representing the envelope curve of actual biases of AOT at 388 nm between the retrieved AOT and AERONET measurements. The forward model parameter errors were analyzed separately for both AOT and SSA retrievals. The surface albedo at 388 nm, the imaginary part of the refractive index at 354 nm, and the number fine mode fraction (FMF) were found to be the most important parameters affecting the retrieval accuracy of AOT, while FMF was the most important parameter for the SSA retrieval. The additional information provided with the retrievals, including the estimated error and degrees of freedom, is expected to be valuable for future studies.


## 1 Introduction

Anthropogenic aerosols have affected both the radiative and meteorological balance in the atmosphere and thus the radiative forcing of the atmosphere directly and indirectly (Ramanathan et al., 2001; Russell et al., 1999; Breon et al., 2002). To understand the





ACPD
15, 16615–16654, 2015

role of aerosol in the atmosphere from a global perspective, reliable aerosol data from satellites are essential (Al-Saadi et al., 2005; Kinne et al., 2006). The several satellite-based methods based on multi-wavelength (Levy et al., 2007; Kim et al., 2007), multi-angle (Fisher et al., 2014), active light (Young et al., 2013), and polarization (Deuze et al., 2001) measurements have their own advantages and limitations. An important advantage of using the ultraviolet (UV) channel to retrieve aerosol optical properties is that the results are less affected by uncertainties in surface reflectance (Torres et al., 1998). The retrieved aerosol products have relatively uniform quality over both land and ocean except over ice–snow surfaces (Torres et al., 2007; Herman et al., 1997). The near-UV technique for aerosol remote sensing has the additional merit of a long term data record including aerosol absorption properties of over 30 years starting from the launch of the Total Ozone Mapping Spectrometer (TOMS) on Nimbus-7 in 1978 (Torres et al., 1998, 2002a, 2005). Thus, the retrieved products using the near-UV technique from TOMS and Ozone Monitoring Instrument (OMI) measurements are appropriate for climatological research (Torres et al., 2002b, 2007). Information on aerosol extinction and absorption properties in the UV region is also important for estimating the air mass factor (AMF) for trace gas retrievals (Palmer et al., 2001; Lin et al., 2014).

Error analysis and characterization of the retrieved products are essential not only for improvement of the retrieval algorithms but also for studies using the retrieval products (Rodgers, 2000). Accuracy assessments of the retrieved aerosol optical properties using UV radiances have been performed by comparison with results from reference methods including ground, airborne, and satellite based remote sensing techniques (Torres et al., 2002a, 2005; Jethva et al., 2014; Ahn et al., 2008, 2014; Livingston et al., 2009; Curier et al., 2008). The aerosol information content of selected OMI spectral radiances using a multi-wavelength algorithm has been estimated using principal component analysis for simulated radiances (Veihelmann et al., 2007). Uncertainty estimates of UV aerosol retrievals have also been calculated by perturbation analysis (Torres et al., 1998, 2002b). Inversion algorithms based on optimal estimation (OE) theory provide not only a constrained solution with respect to the a priori information





ACPD
15, 16615–16654, 2015

but also detailed error analysis from well-categorized error sources (Rodgers, 2000). Recently developed OE-based retrieval methods have provided both improved inversion products and error estimates from the aerosol and surface error sources (Wagner et al., 2010; Govaerts et al., 2010; Wurl et al., 2010).

A large amount of aerosol is emitted from both natural and anthropogenic sources in East Asia (Lee et al., 2012). The spatial and temporal variations in aerosol optical properties are significant because of the diverse emission sources and transboundary transport (Jeong et al., 2011). Thus, the assumed aerosol inversion parameters may cause substantial uncertainties in the retrieval. However, there are insufficient ground-based measurements of aerosol optical properties with suitable spatial and temporal coverage in East Asia, despite their importance for global air quality and climate change. The Distributed Regional Aerosol Gridded Observation Network Northeast Asia (DRAGON-NE Asia) 2012 campaign (http://aeronet.gsfc.nasa.gov/new_web/DRAGON-Asia_2012_Japan_South_Korea.html) provides valuable datasets including both urban and regional-scale observations at more than 40 sites in Northeast Asia. In the present study, an OE-based near-UV aerosol retrieval and error analysis algorithm is developed to provide both improved aerosol inversion products and estimates of their uncertainties. The retrieved aerosol products and estimated uncertainties are validated against the DRAGON-NE Asia 2012 campaign measurements.

## 2 Data

OMI is a nadir-viewing hyperspectral spectrometer aboard the EOS (Earth Observing System)-Aura spacecraft that measures upwelling radiances from the top of the atmosphere in the ultraviolet and visible (270–500 nm) regions with approximate spectral resolution of 0.5 nm (Levelt et al., 2006). The advantage of using OMI for aerosol retrieval is its higher spatial resolution than other UV hyperspectral spectrometers (from $13 \times 24\,\mathrm{km}^2$ at nadir to $28 \times 150\,\mathrm{km}^2$ at the swath extremes with median pixel size $15 \times 32\,\mathrm{km}^2$) together with its 2600 km wide swath. The radiometric calibration procedure and the estimated accuracy of OMI are described in Dobber et al. (2006). To determine aerosol type and vertical distribution, the current OMI near-UV aerosol algorithm (OMAERUV) employs the Cloud–Aerosol Lidar with Orthogonal Polarization (CALIOP) monthly climatology of aerosol layer height and real-time Atmospheric Infrared Sounder (AIRS) carbon monoxide (CO) observations (Torres et al., 2013). Surface reflectances at 354 and 388 nm were assumed to be Lambertian and were taken from the TOMS climatology database. Aerosol vertical distribution and surface reflectance information identical to that used in the operational algorithm were used for the OE-based algorithm here.

In this study, the spatial and temporal domains for analysis were confined to the DRAGON-NE Asia 2012 campaign as shown in Fig. 1 and Table 1. The gridded observation networks had high spatial resolution over the representative megacities in Northeast Asia: Seoul in South Korea and Osaka in Japan. To validate and compare the retrieved aerosol products from OMI, level 2 campaign products were used from the aerosol robotic network (AERONET); 380 nm aerosol optical thickness (AOT) from direct sun measurements and spectral single scattering albedo (SSA) from almucantar inversion products (Holben et al., 1998; Dubovik and King, 2000; Dubovik et al., 2000, 2006). Retrieved 388 nm AOT from OMI was validated against AERONET 380 nm AOT. The OMI AOT retrievals within a radius of 0.5° of the AERONET site and within ± 30 min of the OMI overpass time (about 13:40 LT) were averaged. The resulting OMI AOT average values were then compared with the time-averaged Sun photometer measurements.

Aerosol absorption properties are retrieved at different wavelengths by AERONET and OMI. The AERONET inversion products of the SSA are available at 440, 670, 860, and 1020 nm, while the OMAERUV algorithm retrieves the SSA at 354 and 388 nm. Earlier field studies found that aerosol absorption is a continuous function of wavelength in the ultraviolet to short infrared region (Kirchstetter et al., 2004; Russell et al., 2010). To compare the SSA values from OMI and AERONET at the same wavelength, the AERONET SSA at 388 nm was obtained by extrapolating the SSAs at 440–1020 nm using a spline function. Then the converted AERONET SSA at 388 nm was compared with the retrieved OMI SSA values even though uncertainties might exist in the transformation. Unlike the direct sun measurements including AOT, the inversion products of AERONET from almucantar measurements are retrieved less frequently and require appropriate atmospheric conditions for AOT (440 nm AOT > 0.4) and solar zenith angle (solar zenith angle > 45°) (Dubovik and King, 2000; Jethva et al., 2014). Such favorable atmospheric conditions for the inversion using almucantar measurements rarely overlap closely with the OMI overpass time. Furthermore, too narrow a time window around the satellite overpass time reduces the number of comparison samples. In this study, to secure enough data points the SSA of a region at OMI overpass time was assumed to adequately represent the daily values. For the comparison, the converted 388 nm SSA from AERONET was averaged over a day and the OMI retrievals of 388 nm SSA were spatially averaged over a grid area of 0.5° × 0.5° centered on the AERONET site.

# 3 Method

## 3.1 Operational OMI near UV aerosol algorithm

The OMAERUV uses two channel radiances at 354 and 388 nm to estimate aerosol amount and absorption properties (Torres et al., 1998, 2007, 2013). AOT and SSA at 388 nm are retrieved from pre-calculated reflectance look-up tables (LUT) for predetermined nodal points of observational geometry and aerosol optical properties, total optical depth, and aerosol layer height. Three major aerosol types are considered and listed in Table 2: desert dust, carbonaceous aerosols associated with biomass burning, and weakly absorbing sulfate-based aerosols (hereafter dust, smoke, and sulfate, respectively). Each aerosol type has an assumed particle size distribution (PSD) derived from the long-term statistics of AERONET inversion products. The UV real refractive index ($n_r$) is obtained from the Optical Properties Of Aerosols And Clouds (OPAC) database (Hess et al., 1998). In the operational algorithm, the imaginary refractive indices ($n_i$) at 354 nm are assumed to be 1.0, 1.2, and 1.4 times the retrieved $n_i$ at 388 nm for sulfate, smoke, and dust aerosol, respectively (Torres et al., 2007; Jethva and Torres, 2011). The overall concept and design of the improved OMAERUV algorithm is well described by Torres et al. (2013).

There have been further improvements at updated OMAERUV (version 1.5.3), which was used for reprocessing the data of AOT and SSA in this study. The OMAERUV algorithm was refined by adjusting thresholds of UV aerosol index (UVAI) and Atmospheric Infrared Sounder (AIRS) CO data in determining aerosol types and retrieval approaches. A cloud screening scheme in assigning algorithm quality flags was also modified for retaining more good retrievals of carbonaceous and sulfate type aerosols when the CO level is high enough (higher than $3.2 \times 10^{18}$ molecules cm$^{-2}$) with various reflectivity thresholds. The UVAI threshold was changed from 0.8 to 0.5 over the oceans. This modification eliminates the land-ocean discontinuity in UVAI threshold. It is now identical (0.5) for both conditions. The current characterization of ocean reflective properties in the OMAERUV algorithm does not explicitly account for ocean color effects and, therefore, the quality of the retrieved aerosol properties over the oceans for low aerosol amounts would be highly uncertain. For that reason, retrievals over the oceans are only carried out for high concentrations of either desert dust or carbonaceous aerosols as indicated by UVAI values larger than or equal to 0.5.

Depending on the magnitude of the UVAI and CO parameters as well as the aerosol type, two retrieval approaches are currently used. They are referred to as two-channel and single-channel retrievals. In the two-channel approach, observations at 354 and 388 nm are used to simultaneously derive AOD and SSA. Over scenes when the aerosol absorption signal is low, the single-channel retrieval is applied. AOD is retrieved from the 388 nm observation assuming a value of 1.0 for SSA. Different CO threshold values are used for the northern and Southern Hemispheres to remove upper tropospheric CO which may not be necessarily associated with carbonaceous aerosols. A smoothing function in CO is used to transition from SH to NH threshold values. Specific criteria for retrieval approaches are summarized in Table 3. A more detailed





ACPD
15, 16615–16654, 2015

information of the latest update in OMAERUV is available from the Readme file at the web site (http://disc.sci.gsfc.nasa.gov/Aura/data-holdings/OMI/omaeruv_v003.shtml).

### 3.2 OE-based OMI near UV aerosol algorithm

The traditional LUT-based inversion method potentially includes errors due to interpolation between the nodal points and the local minimum, despite its high numerical efficiency. Online calculation methods (iterative methods) can reduce such errors from interpolation and local minima by employing additional constraints to find more reliable and stable solutions (Kalman, 1960; Phillips, 1962; Tikhonov, 1963; Twomey, 1963; Chahine, 1968). In addition, optimization for measurement error, the inclusion of a priori and ancillary data, and employing physical constraints (e.g., non-negativity of measurements and retrievals) for an inversion method are important since each method has its own advantages and disadvantages (Dubovik, 2004). In this study, we used OE as the inversion method (Rodgers, 2000) since it has several advantages over other methods for OMI-like measurements, as discussed in Sect. 4.

The atmospheric inverse problem often suffers from both insufficient information content of the measurements and imperfect measurement accuracy. Bayesian statistics provides mapping methods from the measurement probability density function (pdf) into state space with prior knowledge. Based on Bayes' theorem, the OE technique employs additional constraints from external sources (a priori) to complement the insufficient information content of the measurements. For the nonlinear inversion case, by considering the maximum a posteriori approach, the general form of the Bayesian solution can be expressed as Eq. (1) where measurement and a priori errors are assumed to be Gaussian (Rodgers, 2000):

$$-2\ln P\left(\boldsymbol{x}|\boldsymbol{y}\right) = [\boldsymbol{y}-\mathbf{K}\boldsymbol{x}]^{\mathrm{T}}\mathbf{S}_{\epsilon}^{-1}[\boldsymbol{y}-\mathbf{K}\boldsymbol{x}] + \left[\boldsymbol{x}-\boldsymbol{x}_{\mathrm{a}}\right]^{\mathbf{T}}\mathbf{S}_{\mathrm{a}}^{-1}\left[\boldsymbol{x}-\boldsymbol{x}_{\mathrm{a}}\right] + \boldsymbol{c} \tag{1}$$

where $\boldsymbol{x}$ is the state vector and $\boldsymbol{y}$ the measurement vector, $\mathbf{K}$ is the weighting function matrix, $\mathbf{S}_{\epsilon}$ is the measurement error covariance matrix, $\boldsymbol{x}_{\mathrm{a}}$ is the a priori mean state,





ACPD
15, 16615–16654, 2015
An online aerosol retrieval algorithm
U. Jeong et al.

and $\mathbf{S}_a$ is the a priori covariance matrix. The formulation finds the optimized solution that minimizes the cost function:

$$\chi^2 = \left\| \mathbf{S}_\epsilon^{-\frac{1}{2}} (\boldsymbol{y} - \mathbf{K}\boldsymbol{x}) \right\|_2^2 + \left\| \mathbf{S}_a^{-\frac{1}{2}} (\boldsymbol{x} - \boldsymbol{x}_a) \right\|_2^2 \tag{2}$$

Detailed derivations and implications are described in previous studies (Rodgers, 2000; Wurl et al., 2010; Govaerts et al., 2010). As described above, the OMI near-UV algorithm uses radiance, $I_{388}$ and spectral contrast, and $I_{354}/I_{388}$ for the measurement vector, where $I_{354}$ and $I_{388}$ are the normalized radiances at 354 and 388 nm, respectively. The state vector in this study is the AOT at 388 nm ($\tau_{388}$) and the imaginary refractive index at 388 nm ($n_{i,388}$). Then, the weighting function matrix can be expressed as follows:

$$\mathbf{K} = \begin{bmatrix} \frac{\partial I_{388}}{\partial \tau_{388}} & \frac{\partial I_{388}}{\partial n_{i,388}} \\ \frac{\partial}{\partial \tau_{388}} \left( \frac{I_{354}}{I_{388}} \right) & \frac{\partial}{\partial n_{i,388}} \left( \frac{I_{354}}{I_{388}} \right) \end{bmatrix} \tag{3}$$

where the weighting function of the spectral contrast can be obtained from the following derivative:

$$\frac{\partial}{\partial \boldsymbol{x}} \left( \frac{I_{354}}{I_{388}} \right) = \frac{\frac{\partial I_{354}}{\partial \boldsymbol{x}} I_{388} - I_{354} \frac{\partial I_{388}}{\partial \boldsymbol{x}}}{(I_{388})^2} \tag{4}$$

In typical inversion methods, including OE, estimation of the reliable measurement error covariance matrix is important to determine the likelihood of the solution (Govaerts et al., 2010). The measurement error includes radiometric noise error and calibration accuracy. The absolute bidirectional scattering distribution function (BSDF) radiometric accuracy of the OMI instrument is reported to be about 4 % for $2\sigma$ and the random noise error is provided in the level 1b product (Dobber et al., 2006). The absolute radiometric uncertainties at each wavelength were calculated from the square root of the sum of squared radiometric random noise and calibration accuracy. The error covariance matrix can be written as:

$$\mathbf{S}_{\epsilon} = \begin{bmatrix} \sigma(\epsilon_{388}) & \sigma(\epsilon_{388}, \epsilon_{354/388}) \\ \sigma(\epsilon_{388}, \epsilon_{354/388}) & \sigma(\epsilon_{354/388}) \end{bmatrix} \tag{5}$$

where $\epsilon_{\lambda}$ is the absolute uncertainty of the measured radiance at wavelength $\lambda$, $\epsilon_{354/388}$ is the uncertainty of $I_{354}/I_{388}$, which is described later in this section, and $\sigma\left(\epsilon_{388}, \epsilon_{354/388}\right)$ is the covariance between the total measurement errors of $I_{388}$ and $I_{354}/I_{388}$.

The $\epsilon_{\lambda}$ typically includes both random and systematic components, and can be expressed as follows:

$$\epsilon_{\lambda} = \epsilon_{\mathrm{r},\lambda} + \epsilon_{\mathrm{s},\lambda} \tag{6}$$

where $\epsilon_{\mathrm{r},\lambda}$ and $\epsilon_{\mathrm{s},\lambda}$ are the random and systematic components of radiometric error at $\lambda$, respectively. The $\epsilon_{354/388}$ can be approximated as follows:

$$\begin{aligned} \epsilon_{354/388} &\cong \frac{I_{354}}{I_{388}} - \frac{I_{354} + \epsilon_{354}}{I_{388} + \epsilon_{388}} \cong \frac{I_{354}}{I_{388}} \left( \frac{\epsilon_{354}}{I_{354}} - \frac{\epsilon_{388}}{I_{388}} \right) \\ &\cong \frac{I_{354}}{I_{388}} \left( \frac{\epsilon_{\mathrm{s},354}}{I_{354}} - \frac{\epsilon_{\mathrm{s},388}}{I_{388}} + \frac{\epsilon_{\mathrm{r},354}}{I_{354}} - \frac{\epsilon_{\mathrm{r},388}}{I_{388}} \right) \end{aligned} \tag{7}$$

When the systematic components of the measurement errors of radiances at 354 and 388 nm are positively correlated and their values are similar, part of the systematic uncertainties can be reduced by the $\frac{\epsilon_{\mathrm{s},354}}{I_{354}} - \frac{\epsilon_{\mathrm{s},388}}{I_{388}}$ term. However, assessment of the systematic error of OMI measurements at each pixel is still challenging despite this partial reduction of systematic errors by using $I_{354}/I_{388}$. In this study, the BSDF calibration uncertainties of $I_{354}$ and $I_{388}$ at a pixel are assumed to be systematic and similar, while the radiometric noise values of $I_{354}$ and $I_{388}$ are assumed to be random and independent. Then, the systematic measurement error of $\epsilon_{354/388}$ can be regarded as negligible and Eq. (7) can be approximated as follows:

$$\sigma\left(\epsilon_{354/388}\right)^{\frac{1}{2}} \cong \frac{I_{354}}{I_{388}}\sqrt{\left(\frac{\epsilon_{\mathrm{r},354}}{I_{354}}\right)^2 + \left(\frac{\epsilon_{\mathrm{r},388}}{I_{388}}\right)^2} \tag{8}$$

where $\epsilon_{\mathrm{r},354}$ and $\epsilon_{r,388}$ represent the radiometric random noise at 354 and 388 nm, respectively.

The $\sigma\left(\epsilon_{388},\epsilon_{354/388}\right)$ can be obtained as follows:

$$\sigma\left(\epsilon_{388},\epsilon_{354/388}\right) = \frac{1}{n-1}\sum_{i=1}^{n}\epsilon_{388}^{\prime i}\epsilon_{354/388}^{\prime i} \tag{9}$$

where $\epsilon_{388}^{\prime i}$ and $\epsilon_{354/388}^{\prime i}$ are the uncertainties in the $i$th measurement of $I_{388}$ and $I_{354}/I_{388}$ for a sample of size $n$, respectively. Under the same assumptions used in Eqs. (7) and (8), $\epsilon_{354/388}^{\prime i}$ has only random and independent components, and so $\sigma\left(\epsilon_{388},\epsilon_{354/388}\right)$ can be regarded as negligible. The diagonal and off-diagonal elements of the measurement error covariance matrices using two different measurement matrices are compared in Table 4.

### 3.3 Error characterization

Retrieved products with estimated and/or characterized error are valuable for any application. Various error sources can be categorized as shown in the following equation by linearizing the forward model with respect to associated parameters (Eyre, 1987; Rodgers, 1990, 2000):

$$\hat{\boldsymbol{x}} - \boldsymbol{x} = (\mathbf{A} - \mathbf{I}_n)(\boldsymbol{x} - \boldsymbol{x}_\mathrm{a}) + \mathbf{G}_y\mathbf{K}_b\left(\boldsymbol{b} - \hat{\boldsymbol{b}}\right) + \mathbf{G}_y\Delta f\left(\boldsymbol{x},\boldsymbol{b},\boldsymbol{b}'\right) + \mathbf{G}_y\epsilon \tag{10}$$

where $\hat{\boldsymbol{x}}$ and $\boldsymbol{x}$ are the retrieval and true states, respectively; $\mathbf{A}$ is the averaging kernel matrix; $\mathbf{I}_n$ is the identity matrix; $\boldsymbol{x}_\mathrm{a}$ is the a priori state vector; $\mathbf{G}_y$ is the contribution





ACPD
15, 16615–16654, 2015

An online aerosol retrieval algorithm

U. Jeong et al.

function matrix; $\mathbf{K}_b$ is the weighting function matrix of forward model parameters ($\boldsymbol{b}$); $\hat{\boldsymbol{b}}$ is the guessed forward model parameter; $\Delta f$ is the error in the forward model relative to the real physics; and $\epsilon$ is the measurement error. The first and last term on the right-hand-side (RHS) of Eq. (10) is the smoothing error and retrieval noise, respectively. Their covariance matrices can be calculated from:

$$\mathbf{S}_\mathrm{s} = (\mathbf{A} - \mathbf{I}_n)\mathbf{S}_\mathrm{E}(\mathbf{A} - \mathbf{I}_n)^\mathrm{T} \tag{11}$$

$$\mathbf{S}_\mathrm{n} = \mathbf{G}_y \mathbf{S}_\epsilon \mathbf{G}_y^\mathrm{T} \tag{12}$$

where $\mathbf{S}_\mathrm{s}$ is the smoothing error covariance matrix, $\mathbf{S}_\mathrm{E}$ is the covariance of the ensemble of states about the mean state, and $\mathbf{S}_\mathrm{n}$ is the covariance matrix of the retrieval noise. We have assumed that the climatological value is a good representation of the real ensemble of the state about the mean state, and so the covariance matrix of the a priori state was employed as the $\mathbf{S}_\mathrm{E}$ in this study. Each $\mathbf{S}_\mathrm{s}$ and $\mathbf{S}_\mathrm{n}$ has two diagonal elements that represent the variances of the smoothing error and retrieval noise for two retrievals, AOT and SSA. The smoothing error ($\mathbf{S}_\mathrm{s}$) and retrieval noise ($\mathbf{S}_\mathrm{n}$) of AOT and SSA were defined as the square root of the corresponding diagonal elements of $\mathbf{S}_\mathrm{s}$ and $\mathbf{S}_\mathrm{n}$, respectively. The square root of the sum of squared $\mathbf{S}_\mathrm{s}$ and $\mathbf{S}_\mathrm{n}$ of AOT and SSA are defined in this study as the solution errors ($\mathbf{S}_\mathrm{sn}$) of AOT and SSA, respectively.

The second term on the RHS of Eq. (10) is the forward model parameter error, and its covariance matrix can be calculated as follows:

$$\mathbf{S}_\mathrm{f} = \mathbf{G}_y \mathbf{K}_b \mathbf{S}_b \mathbf{K}_b^\mathrm{T} \mathbf{G}_y^\mathrm{T} \tag{13}$$

where $\mathbf{S}_\mathrm{f}$ is the forward model parameter error covariance matrix, and $\mathbf{S}_b$ is the error covariance matrix of forward model parameter $b$. The forward model parameters of the near-UV method include the aerosol microphysical model parameters, aerosol vertical distribution, meteorological profile (pressure and temperature), and surface properties. These forward model parameters contain both random and systematic components with different scales of spatial and temporal variation. Furthermore, each forward model parameter has a different uncertainty that is difficult to evaluate. In this study, $\mathbf{S}_\mathrm{f}$ was analyzed separately with respect to each forward model parameter as suggested by Rodgers (2000).

The third term on the RHS in Eq. 10 is the forward model error that is caused by discrepancies between known and real physics. To simulate the earth-reflected radiance, VLIDORT (linearized pseudo-spherical vector discrete ordinate radiative transfer code, version 2.6) was used. This code is based on one of the most accurate radiative transfer solutions for a one-dimensional atmosphere (Spurr, 2006). Linearization of state vectors and forward model parameters are described in Spurr et al. (2012) and Spurr and Christi (2014). Although the simulated radiances are expected to be accurate, the forward model error depends on factors including the number of streams, layers, and Legendre coefficients for the aerosol phase functions. To reduce the numerical errors that can arise from an insufficient number of coefficients, 3 Stokes parameters, 75 layers, 16 streams, and up to 500 Legendre coefficients for the aerosol phase matrix were used for the radiance simulations. However, it is still a challenge to evaluate other possible sources of forward model error such as Raman scattering and the three-dimensional effect of the atmosphere for retrieval. Such issues are beyond the scope of this study, and thus only smoothing error, retrieval noise, and forward model parameter error are evaluated here.

### 3.4 A priori characterization

Using reliable a priori information is important in the OE method since the final solutions are determined between the a priori state and the inversion space of a measurement. There are several sources of a priori information including climatological data, reliable measurements from more accurate instruments, and calculations from models based on theoretical or empirical statistics (Govaerts et al., 2010; Wurl et al., 2010; Rodgers, 2000). Appropriate sources of a priori depend on the characteristics of the state vector and the accuracy of the a priori database. When the a priori state has a systematic bias away from the true state, this bias propagates to the retrieval products. In this





ACPD
15, 16615–16654, 2015

study, 10 years (from 2005 to 2014) of OMAERUV 388 nm AOT and SSA in spring (from March to May) were used for the a priori data. Figure 2 shows the collected climatological data of the 388 nm AOT and SSA in East Asia used in this study. To avoid biases due to cloud contamination in the OMI products, averaged values and standard deviations ($\sigma$) with more than 70 data points were used.

## 4 Results

The dust event on 28 April 2012 has been selected to compare the aerosol optical properties from the operational product with the OE-based retrievals in this study. Figure 3 shows the true color image on that day from the Moderate Resolution Imaging Spectroradiometer (MODIS) Aqua and the UV aerosol index from OMI. To see the difference between the OE-based and operational algorithm in the same area, both methods were applied to measurements with an operational algorithm flag of 0, to avoid cloud contamination and radiometric calibration uncertainties. Some of the points retrieved by the operational algorithm were rejected in the OE-based retrievals when the cost function cut-off was applied, as described in this section.

The AOT and SSA at 388 nm from the operational and OE-based products are compared in Fig. 4. The $\mathbf{S}_{\mathrm{sn}}$ of the retrieved AOT and SSA at 388 nm, degree of freedom, and cost function are shown in Fig. 5. The OE-based and operational AOT at 388 nm are similar, as shown in Fig. 4a and b. Both products seem to be affected by snow and cloud contaminated pixels around Seoul in South Korea (37° N, 126° E), Tianjin in China (39° N, 116° E) and Nagano in Japan (36° N, 138° E). In Fig. 5a, the $\mathbf{S}_{\mathrm{sn}}$ of retrieved AOT at 388 nm has relatively high values compared with the AOT level at large viewing zenith angle. Noticeable discrepancies of SSA at 388 nm from the operational and OE-based products are evident in some of the areas as shown in Fig. 4c and d. The operational algorithm performed single-channel retrieval around East Mongolia (36° N, 138° E), while the OE-based algorithm performed two-channel retrieval for all cases. Since this area has a low level of AOT, the information content of aerosol





ACPD
15, 16615–16654, 2015

absorption property is insufficient, resulting in the low degrees of freedom shown in Figs. 4b and 5c. Thus the OE-based SSA in this area (Fig. 4d) seems noisy and the $\mathbf{S}_{sn}$ of SSA appears high. Similar results for the behavior of SSA are apparent around central Japan (38° N, 138° E). Thus, SSA values with high AOT and low $\mathbf{S}_{sn}$ are recommended for the analysis, similar to the retrieval conditions for AERONET inversion products (Dubovik and King, 2000). Additional information provided on retrievals at each pixel in Fig. 5 is expected to be valuable for relevant studies including trace gas retrieval and data assimilation.

Figure 6 shows the results of validation of operational and OE-based AOT retrievals at 388 nm. As shown in Fig. 6a and b, the OE-based inversion method showed higher correlation ($r = 0.82$) and slightly improved slope (0.81) and offset (0.17) values than the operational algorithm ($r = 0.71$, slope = 0.71, and offset = 0.2). The $Q$ values (percentage of AOT retrievals falling within an uncertainty envelope of ±30 % or 0.1) of the OE-based retrievals (62.2 %) and operational algorithm (63.0 %) were comparable. When a measured radiance is affected by parameters that the theoretical radiative transfer model does not consider (e.g., sub-pixel cloud contamination), the cost function of the retrieval typically has a high value. In this study, retrievals with cost function ($\chi$) larger than a certain value ($\sqrt{2}$ in this study) have been rejected. This limitation on retrievals imposed by the cost function reduced the number of retrievals with abnormally high biases, which might be associated with sub-pixel cloud contamination, in the operational algorithm in Fig. 6a.

The SSA values at 388 nm from OMI operational products and OE-based inversion products were compared with those at 388 and 440 nm from AERONET inversion products as shown in Fig. 7. The cost function limitation also removed retrievals with abnormal biases in SSA (compare Fig. 7a and b, or c and d). However, the retrieved SSA at 388 nm from the operational algorithm showed higher values of $Q_{0.03}$ (59.2 %) and $Q_{0.05}$ (85.1 %) than those from the OE-based algorithm ($Q_{0.03}$ = 53.8 %, $Q_{0.05}$ = 84.4 %) when compared with the AERONET SSA at 440 nm (the $Q_{0.03}$ and $Q_{0.05}$ represent the percentage of SSA retrievals falling within an uncertainty envelope of ± 0.03 and

± 0.05, respectively). The retrieved 388 nm SSA from both the operational and OE-based algorithms showed similar correlation ($r = 0.27$ and 0.26 for operational and OE-based algorithms, respectively). The retrieved SSA at 388 nm from the operational and OE-based algorithms were more highly correlated with the converted 388 nm SSA from AERONET ($r = 0.34$ for both the operational and OE-based algorithm) than with the 440 nm SSA from AERONET. The retrieved SSA at 388 nm from the operational algorithm also showed higher values of $Q_{0.03}$ (59.2 %) and $Q_{0.05}$ (83.9 %) than those of the OE-based algorithm ($Q_{0.03}$ = 56.9 %, $Q_{0.05}$ = 81.9 %) when compared with converted SSA at 388 nm from AERONET.

The estimated solution errors of the AOT at 388 nm from the operational algorithm and the OE-based method were plotted against the biases relative to AERONET measurements as shown in Fig. 8. The percentages of AOT retrieval biases from AERONET falling within the estimated solution errors ($Q_{se}$) were 84.8 and 85.8 % for the operational algorithm and the OE-based method, respectively. Their envelope curves were generally well represented by the estimated solution error line except for several points that might be related to other error sources, including forward model parameters and forward model errors. Since the estimated uncertainty of retrieved AOT using the OE method considers the theoretical sensitivity of the retrieval biases to associated parameters, it explained the retrieval uncertainties better than the traditional error estimation method, which only considers the retrieved AOT values ($Q_{se} > Q$). As shown in Fig. 8b, $\mathbf{S}_{sn}$ is generally proportional to retrieved AOT but it cannot be explained by AOT alone. The 388 nm AOT retrievals of the operational algorithm, which contain high biases, were reduced as shown in Fig. 8b.

Table 5 shows the suggested error sources and their magnitudes from the OMI ATBD (Algorithm Theoretical Basis Documents) (Torres et al., 2002b) and the values employed in this study. Although the current OMI cloud masking method is based on long-term TOMS heritage, there may still be ground pixels contaminated by sub-pixel clouds. As the TOA reflectance is greatly increased by even a small amount of cloud, cloud contamination can cause large positive biases in the AOT retrieval. Previous studies esti-





ACPD
15, 16615–16654, 2015



Title Page
Abstract | Introduction
Conclusions | References
Tables | Figures
◀ | ▶
Back | Close
Full Screen / Esc
Printer-friendly Version
Interactive Discussion

mated the AOT retrieval errors due to 5 % cloud contamination to be of the order of 0.1 to 0.2 (Torres et al., 1998, 2002b). They also reported an even higher error in the single scattering albedo (0 to 0.15) especially for strongly absorbing aerosols. However, estimation of sub-pixel cloud contamination is difficult because of the large spatio-temporal variability of clouds and the relatively large ground pixel size of OMI. Thus the further error analysis in Torres et al. (2002b) was not performed in this study. Typical uncertainties of the 354 and 388 nm surface reflectances were assumed to be 0.01 for both land and ocean. Radiometric uncertainties were taken from recently reported values by Dobber et al. (2006), and radiometric precision from OMI Level 1b data. To analyze the uncertainty associated with the aerosol size information and refractive index, $\sigma$ values of the size parameter and $n_r$ at 440 nm were taken from AERONET inversion products during the campaign period. To analyze the assumed $n_i$ at 354 nm, the $\mathbf{S}_b$ was also obtained from AERONET climatology during the campaign period. Aerosol vertical distribution is important as it affects aerosol retrieval using near-UV and blue channels, particularly for absorbing aerosols (Torres et al., 1998, 2013; de Graaf et al., 2005). However, accuracy assessments of the aerosol height information used are still challenging. Typical uncertainties of the assumed aerosol layer peak height and half width were assumed to be 2 and 1 km, respectively, in this study. In the OE-based near-UV aerosol retrieval algorithm, all aerosols are assumed to be spherical and the optical properties are calculated from aerosol microphysical properties using the Mie solution. However, non-sphericity may cause significant uncertainties, especially for large particles (Mishchenko and Travis, 1994; Mishchenko et al., 1995, 1997, 2003; Dubovik et al., 2006), and aerosol morphology is quite complicated and requires further analysis for the near-UV region. This is out of the scope of this study and thus needs to be investigated in a future study. Therefore the uncertainties due to aerosol non-sphericity were not analyzed.

Figure 9 shows the average and $\sigma$ values of forward model parameter errors of the retrieved AOT and SSA that were sampled for the validation in Figs. 6b and 7b and d. High values of forward model parameter error for AOT appeared in $n_i$ at 354 nm

(0.27 ± 0.25), number fine mode fraction (FMF) (0.26 ± 0.14), and the surface albedo at 388 nm (0.16 ± 0.06). These values are comparable with the mean $\mathbf{S}_{sn}$ of retrieved AOT at 388 nm (0.34). Thus, the accuracy of AOT retrievals depends on not only the radiometric accuracy and information content but also the aerosol models and ancillary data of the surface albedo, of which the effect is already well known. The FMFs of the sulfate (0.999596) and smoke type aerosols (0.999795) are similar while that for dust type aerosols is quite different (0.995650). Considering that the estimated $\sigma$ value for FMF uncertainty in this study (0.0015, see Table 5) is much lower than the difference between the FMFs of dust type and other aerosols (~ 0.004, see Table 2), the errors resulting from selection of the wrong aerosol type can be more significant. The estimated forward model parameter error of the surface reflectance at 388 nm was higher than the previously suggested value (0.07–0.09 for AOT and < 0.01 for SSA) in the OMI ATBD (Torres et al., 2002b). The forward model parameter errors of AOT with respect to the surface albedo at 354 nm (0.08 ± 0.03), peak height of the aerosol vertical distribution (0.07 ± 0.08), fine mode $n_r$ (0.07 ± 0.08), mean radius of the coarse mode PSD (0.08 ± 0.04), and half width of the fine mode PSD (0.06 ± 0.05) showed similar moderate sensitivity. Those for the half width of the aerosol vertical distribution (0.04 ± 0.05), mean radius of the fine mode PSD (0.02 ± 0.02) and half width of the coarse mode PSD (0.03 ± 0.01) were smaller and that of the coarse mode $n_r$ (0.004 ± 0.01) was found to be negligible.

Among the forward model parameter errors of the SSA retrieval, the FMF error ($8.3 \times 10^{-3} \pm 5.7 \times 10^{-3}$) was the most important of the forward model parameter errors of the SSA retrieval. Errors in $n_i$ at 354 nm ($4.2 \times 10^{-3} \pm 2.2 \times 10^{-3}$) and the peak height of the aerosol vertical distribution ($3.0 \times 10^{-3} \pm 2.0 \times 10^{-3}$) were found to be the second most important. The forward model parameter error of SSA with respect to the surface reflectance at 354 nm ($1.6 \times 10^{-3} \pm 7.0 \times 10^{-4}$) and 388 nm ($1.2 \times 10^{-3} \pm 7.3 \times 10^{-4}$), half width of the aerosol vertical distribution ($1.3 \times 10^{-3} \pm 8.9 \times 10^{-4}$), the fine mode $n_r$ ($2.3 \times 10^{-3} \pm 1.5 \times 10^{-3}$), mean radius of the fine mode PSD ($7.4 \times 10^{-4} \pm 1.1 \times 10^{-3}$), mean radius of the coarse mode PSD ($2.1 \times 10^{-3} \pm 2.7 \times 10^{-3}$), width of the fine mode





ACPD
15, 16615–16654, 2015

PSD ($2.3\times10^{-3}\pm1.4\times10^{-3}$, and width of the coarse mode PSD ($6.2\times10^{-4}\pm 9.0\times10^{-4}$) were smaller and that of the coarse mode $n_r$ ($7.2\times10^{-5}\pm3.2\times10^{-4}$) appeared to be negligible. The estimated forward model parameter errors of SSA were found to be about an order magnitude lower than the $\mathbf{S}_{sn}$ of SSA. The mean $\mathbf{S}_s$ of SSA (0.05) was higher than the mean $\mathbf{S}_n$ of SSA (0.03) since the SSA retrieval requires sufficient aerosol signal in the measurements. Thus, the estimated $\mathbf{S}_{sn}$ of SSA at 388 nm is expected to be more reliable and represent the total uncertainties of SSA, since the uncertainty in SSA is predominantly affected by $\mathbf{S}_{sn}$, while uncertainty in AOT is affected by both $\mathbf{S}_{sn}$ and $\mathbf{S}_f$.

## 5 Summary and discussion

An OE-based aerosol retrieval and error characterization algorithm using the OMI near-UV radiances was developed in this study. The climatological values of OMAERUV products were employed as a priori data for the inversion method. The OE-based inversion method developed here provides not only the retrieved values of AOT and SSA but also estimates of their uncertainties. The retrieved AOT and SSA at 388 nm were compared with the AERONET products during the DRAGON-NE Asia 2012 campaign. The retrieved AOT using the OE method showed better results than the operational product. The OE-based SSA at 388 nm showed consistency with AERONET inversion products comparable to that of the operational SSA. The estimated retrieval noise and smoothing error of OE-based AOT represented well the envelope curve of actual biases between the retrieved AOT and AERONET AOT. The forward model parameter errors were analyzed separately for both AOT and SSA inversion products. Uncertainties of surface albedo at 388 nm, imaginary refractive index at 354 nm and number fine mode fraction were found to be the most important parameters affecting the retrieval accuracy of AOT, while uncertainties in the coarse mode real part of the refractive index had negligible effect. For SSA retrieval accuracy, number fine mode fraction was found to be the most important parameter while the other parameters appeared to have relatively small effects. As the FMF depends on the aerosol type, it is expected that more accurate aerosol type classification might improve the retrieval accuracy of AOT and SSA. For AOT retrieval, the estimated $\mathbf{S}_f$ was comparable with the $\mathbf{S}_{sn}$, while the $\mathbf{S}_f$ of SSA was negligible compared to the $\mathbf{S}_{sn}$ of the retrieved SSA. It is also found that a sufficient amount of aerosol loading is necessary for reliable SSA retrieval.

However, there are still error sources which need to be analyzed, including the a priori error from climatology, aerosol morphology, cloud contamination, and three dimensional effects of radiative transfer. The assumed conditions in the inversion procedure also differ from the real state. Validation studies for a longer period at more types of site are also necessary. Securing a more reliable a priori database is expected to improve the OE-based aerosol retrieval algorithm.

*Acknowledgements.* This research was supported by the GEMS program of the Ministry of Environment, Korea and the Eco Innovation Program of KEITI (2012000160002). The authors also acknowledge the KNMI and NASA/GSFC for providing OMI and AERONET data.

## References

Ahn, C., Torres, O., and Bhartia, P. K.: Comparison of ozone monitoring instrument UV aerosol products with aqua/moderate resolution imaging spectroradiometer and multiangle imaging spectroradiometer observations in 2006, J. Geophys. Res.-Atmos., 113, D16S27, doi:10.1029/2007jd008832, 2008.

Ahn, C., Torres, O., and Jethva, H.: Assessment of OMI near-UV aerosol optical depth over land, J. Geophys. Res.-Atmos., 119, 2457–2473, doi:10.1002/2013jd020188, 2014.

Al-Saadi, J., Szykman, J., Pierce, R. B., Kittaka, C., Neil, D., Chu, D. A., Remer, L., Gumley, L., Prins, E., Weinstock, L., MacDonald, C., Wayland, R., Dimmick, F., and Fishman, J.: Improving national air quality forecasts with satellite aerosol observations, B. Am. Meteorol. Soc., 86, 1249, doi:10.1175/Bams-86-9-1249, 2005.

Breon, F. M., Tanre, D., and Generoso, S.: Aerosol effect on cloud droplet size monitored from satellite, Science, 295, 834–838, doi:10.1126/science.1066434, 2002.

Chahine, M. T.: Determination of temperature profile in an atmosphere from its outgoing radiance, J. Opt. Soc. Am., 12, 1634–1637, 1968.
Curier, R. L., Veefkind, J. P., Braak, R., Veihelmann, B., Torres, O., and de Leeuw, G.: Retrieval of aerosol optical properties from OMI radiances using a multiwavelength algorithm: application to western Europe, J. Geophys. Res.-Atmos., 113, D17S90, doi:10.1029/2007jd008738, 2008.
de Graaf, M., Stammes, P., Torres, O., and Koelemeijer, R. B. A.: Absorbing aerosol index: sensitivity analysis, application to GOME and comparison with TOMS, J. Geophys. Res.-Atmos., 110, D01201, doi:10.1029/2004jd005178, 2005.
Deuze, J. L., Breon, F. M., Devaux, C., Goloub, P., Herman, M., Lafrance, B., Maignan, F., Marchand, A., Nadal, F., Perry, G., and Tanre, D.: Remote sensing of aerosols over land surfaces from POLDER-ADEOS-1 polarized measurements, J. Geophys. Res.-Atmos., 106, 4913–4926, doi:10.1029/2000jd900364, 2001.
Dobber, M. R., Dirksen, R. J., Levelt, P. F., Van den Oord, G. H. J., Voors, R. H. M., Kleipool, Q., Jaross, G., Kowalewski, M., Hilsenrath, E., Leppelmeier, G. W., de Vries, J., Dierssen, W., and Rozemeijer, N. C.: Ozone-monitoring instrument calibration, IEEE T. Geosci. Remote, 44, 1209–1238, doi:10.1109/Tgrs.2006.869987, 2006.
Dubovik, O.: Photopolarimetry in remote sensing, in: Mathematics, Physics and Chemistry, edited by: Videen, G., Yatskiv, Y., and Mishchenko, M., 161, Kluwer Academic Publishers, Netherlands, 65–106, 2004.
Dubovik, O. and King, M. D.: A flexible inversion algorithm for retrieval of aerosol optical properties from Sun and sky radiance measurements, J. Geophys. Res.-Atmos., 105, 20673–20696, doi:10.1029/2000jd900282, 2000.
Dubovik, O., Smirnov, A., Holben, B. N., King, M. D., Kaufman, Y. J., Eck, T. F., and Slutsker, I.: Accuracy assessments of aerosol optical properties retrieved from aerosol robotic network (AERONET) sun and sky radiance measurements, J. Geophys. Res.-Atmos., 105, 9791–9806, doi:10.1029/2000jd900040, 2000.
Dubovik, O., Sinyuk, A., Lapyonok, T., Holben, B. N., Mishchenko, M., Yang, P., Eck, T. F., Volten, H., Munoz, O., Veihelmann, B., van der Zande, W. J., Leon, J. F., Sorokin, M., and Slutsker, I.: Application of spheroid models to account for aerosol particle nonsphericity in remote sensing of desert dust, J. Geophys. Res.-Atmos., 111, D11208 doi:10.1029/2005jd006619, 2006.

Eyre, J. R.: On systematic-errors in satellite sounding products and their climatological mean-values, Q. J. Roy. Meteor. Soc., 113, 279–292, doi:10.1002/qj.49711347516, 1987.
Fisher, D., Muller, J. P., and Yershov, V. N.: Automated stereo retrieval of smoke plume injection heights and retrieval of smoke plume masks from AATSR and their assessment with CALIPSO and MISR, IEEE T. Geosci. Remote, 52, 1249–1258, doi:10.1109/Tgrs.2013.2249073, 2014.
Govaerts, Y. M., Wagner, S., Lattanzio, A., and Watts, P.: Joint retrieval of surface reflectance and aerosol optical depth from MSG/SEVIRI observations with an optimal estimation approach: 1. Theory, J. Geophys. Res.-Atmos., 115, D02203 doi:10.1029/2009jd011779, 2010.
Herman, J. R., Bhartia, P. K., Torres, O., Hsu, C., Seftor, C., and Celarier, E.: Global distribution of UV-absorbing aerosols from Nimbus 7/TOMS data, J. Geophys. Res.-Atmos., 102, 16911–16922, doi:10.1029/96jd03680, 1997.
Hess, M., Koepke, P., and Schult, I.: Optical properties of aerosols and clouds: the software package OPAC, B. Am. Meteorol. Soc., 79, 831–844, doi:10.1175/1520-0477(1998)079<0831:Opoaac>2.0.Co;2, 1998.
Holben, B. N., Eck, T. F., Slutsker, I., Tanre, D., Buis, J. P., Setzer, A., Vermote, E., Reagan, J. A., Kaufman, Y. J., Nakajima, T., Lavenu, F., Jankowiak, I., and Smirnov, A.: AERONET – a federated instrument network and data archive for aerosol characterization, Remote Sens. Environ., 66, 1–16, doi:10.1016/S0034-4257(98)00031-5, 1998.
Jeong, U., Kim, J., Lee, H., Jung, J., Kim, Y. J., Song, C. H., and Koo, J. H.: Estimation of the contributions of long range transported aerosol in East Asia to carbonaceous aerosol and PM concentrations in Seoul, Korea using highly time resolved measurements: a PSCF model approach, J. Environ. Monitor., 13, 1905–1918, doi:10.1039/C0em00659a, 2011.
Jethva, H. and Torres, O.: Satellite-based evidence of wavelength-dependent aerosol absorption in biomass burning smoke inferred from Ozone Monitoring Instrument, Atmos. Chem. Phys., 11, 10541–10551, doi:10.5194/acp-11-10541-2011, 2011.
Jethva, H., Torres, O., and Ahn, C.: Global assessment of OMI aerosol single-scattering albedo using ground-based AERONET inversion, J. Geophys. Res.-Atmos., 119, 9020–9040, doi:10.1002/2014jd021672, 2014.
Kalman, R. E.: A new approach to linear filtering and prediction problems, J. Basic Eng.-T. ASME, 82, 35–45, 1960.
Kim, J., Lee, J., Lee, H. C., Higurashi, A., Takemura, T., and Song, C. H.: Consistency of the aerosol type classification from satellite remote sensing during the atmospheric brown





ACPD
15, 16615–16654, 2015

cloud – East Asia regional experiment campaign, J. Geophys. Res.-Atmos., 112, D22S33, doi:10.1029/2006jd008201, 2007.
Kinne, S., Schulz, M., Textor, C., Guibert, S., Balkanski, Y., Bauer, S. E., Berntsen, T., Berglen, T. F., Boucher, O., Chin, M., Collins, W., Dentener, F., Diehl, T., Easter, R., Feichter, J., Fillmore, D., Ghan, S., Ginoux, P., Gong, S., Grini, A., Hendricks, J., Herzog, M., Horowitz, L., Isaksen, I., Iversen, T., Kirkevåg, A., Kloster, S., Koch, D., Kristjansson, J. E., Krol, M., Lauer, A., Lamarque, J. F., Lesins, G., Liu, X., Lohmann, U., Montanaro, V., Myhre, G., Penner, J., Pitari, G., Reddy, S., Seland, O., Stier, P., Takemura, T., and Tie, X.: An AeroCom initial assessment – optical properties in aerosol component modules of global models, Atmos. Chem. Phys., 6, 1815–1834, doi:10.5194/acp-6-1815-2006, 2006.
Kirchstetter, T. W., Novakov, T., and Hobbs, P. V.: Evidence that the spectral dependence of light absorption by aerosols is affected by organic carbon, J. Geophys. Res.-Atmos., 109, D21208, doi:10.1029/2004jd004999, 2004.
Lee, J., Kim, J., Yang, P., and Hsu, N. C.: Improvement of aerosol optical depth retrieval from MODIS spectral reflectance over the global ocean using new aerosol models archived from AERONET inversion data and tri-axial ellipsoidal dust database, Atmos. Chem. Phys., 12, 7087–7102, doi:10.5194/acp-12-7087-2012, 2012.
Levelt, P. F., Van den Oord, G. H. J., Dobber, M. R., Malkki, A., Visser, H., de Vries, J., Stammes, P., Lundell, J. O. V., and Saari, H.: The Ozone Monitoring Instrument, IEEE T. Geosci. Remote, 44, 1093–1101, doi:10.1109/Tgrs.2006.872333, 2006.
Levy, R. C., Remer, L. A., Mattoo, S., Vermote, E. F., and Kaufman, Y. J.: Second-generation operational algorithm: retrieval of aerosol properties over land from inversion of moderate resolution imaging spectroradiometer spectral reflectance, J. Geophys. Res.-Atmos., 112, D13211, doi:10.1029/2006jd007811, 2007.
Lin, J.-T., Martin, R. V., Boersma, K. F., Sneep, M., Stammes, P., Spurr, R., Wang, P., Van Roozendael, M., Clémer, K., and Irie, H.: Retrieving tropospheric nitrogen dioxide from the Ozone Monitoring Instrument: effects of aerosols, surface reflectance anisotropy, and vertical profile of nitrogen dioxide, Atmos. Chem. Phys., 14, 1441–1461, doi:10.5194/acp-14-1441-2014, 2014.
Livingston, J. M., Redemann, J., Russell, P. B., Torres, O., Veihelmann, B., Veefkind, P., Braak, R., Smirnov, A., Remer, L., Bergstrom, R. W., Coddington, O., Schmidt, K. S., Pilewskie, P., Johnson, R., and Zhang, Q.: Comparison of aerosol optical depths from the Ozone Monitoring Instrument (OMI) on Aura with results from airborne sunphotometry, other

space and ground measurements during MILAGRO/INTEX-B, Atmos. Chem. Phys., 9, 6743–6765, doi:10.5194/acp-9-6743-2009, 2009.
Mishchenko, M. I. and Travis, L. D.: T-matrix computations of light-scattering by large spheroidal particles, Opt. Commun., 109, 16–21, doi:10.1016/0030-4018(94)90731-5, 1994.
Mishchenko, M. I., Lacis, A. A., Carlson, B. E., and Travis, L. D.: Nonsphericity of dust-like tropospheric aerosols – implications for aerosol remote-sensing and climate modeling, Geophys. Res. Lett., 22, 1077–1080, doi:10.1029/95gl00798, 1995.
Mishchenko, M. I., Travis, L. D., Kahn, R. A., and West, R. A.: Modeling phase functions for dustlike tropospheric aerosols using a shape mixture of randomly oriented polydisperse spheroids, J. Geophys. Res.-Atmos., 102, 16831–16847, doi:10.1029/96jd02110, 1997.
Mishchenko, M. I., Geogdzhayev, I. V., Liu, L., Ogren, J. A., Lacis, A. A., Rossow, W. B., Hovenier, J. W., Volten, H., and Munoz, O.: Aerosol retrievals from AVHRR radiances: effects of particle nonsphericity and absorption and an updated long-term global climatology of aerosol properties, J Quant. Spectrosc. Ra., 79, 953–972, doi:10.1016/S0022-4073(02)00331-X, 2003.
Palmer, P. I., Jacob, D. J., Chance, K., Martin, R. V., Spurr, R. J. D., Kurosu, T. P., Bey, I., Yantosca, R., Fiore, A., and Li, Q. B.: Air mass factor formulation for spectroscopic measurements from satellites: application to formaldehyde retrievals from the Global Ozone, monitoring, experiment, J. Geophys. Res.-Atmos., 106, 14539–14550, doi:10.1029/2000jd900772, 2001.
Phillips, B. L.: A technique for numerical solution of certain intergral equation of first kind, J. Assoc. Comput. Mach., 9, 84–97, 1962.
Ramanathan, V., Crutzen, P. J., Kiehl, J. T., and Rosenfeld, D.: Atmosphere – aerosols, climate, and the hydrological cycle, Science, 294, 2119–2124, doi:10.1126/science.1064034, 2001.
Rodgers, C. D.: Characterization and error analysis of profiles retrieved from remote sounding measurements, J. Geophys. Res.-Atmos., 95, 5587–5595, doi:10.1029/Jd095id05p05587, 1990.
Rodgers, C. D.: Inverse Method for Atmospheric Sounding: Theory and Practice, World Scientific Publishing Co. Pte. Ltd., Singapore, 2000.
Russell, P. B., Hobbs, P. V., and Stowe, L. L.: Aerosol properties and radiative effects in the United States East Coast haze plume: an overview of the tropospheric aerosol radiative forcing observational experiment (TARFOX), J. Geophys. Res.-Atmos., 104, 2213–2222, doi:10.1029/1998jd200028, 1999.





ACPD
15, 16615–16654, 2015



Title Page
Abstract | Introduction
Conclusions | References
Tables | Figures
◀I | ▶I
◀ | ▶
Back | Close
Full Screen / Esc
Printer-friendly Version
Interactive Discussion

Russell, P. B., Bergstrom, R. W., Shinozuka, Y., Clarke, A. D., DeCarlo, P. F., Jimenez, J. L., Livingston, J. M., Redemann, J., Dubovik, O., and Strawa, A.: Absorption angstrom exponent in AERONET and related data as an indicator of aerosol composition, Atmos. Chem. Phys., 10, 1155–1169, doi:10.5194/acp-10-1155-2010, 2010.

Spurr, R. J. D.: VLIDORT: A linearized pseudo-spherical vector discrete ordinate radiative transfer code for forward model and retrieval studies in multilayer multiple scattering media, J. Quant. Spectrosc. Ra., 102, 316–342, doi:10.1016/j.jqsrt.2006.05.005, 2006.

Tikhonov, A. N.: On the solution of incorrectly stated problems and a method of regularization, Dokl. Akad. Nauk. +, 151, 501–504, 1963.

Torres, O., Bhartia, P. K., Herman, J. R., Ahmad, Z., and Gleason, J.: Derivation of aerosol properties from satellite measurements of backscattered ultraviolet radiation: theoretical basis (Vol. 103, p. 17099, 1998), J. Geophys. Res.-Atmos., 103, p. 23321, 1998.

Torres, O., Bhartia, P. K., Herman, J. R., Sinyuk, A., Ginoux, P., and Holben, B.: A long-term record of aerosol optical depth from TOMS observations and comparison to AERONET measurements, J. Atmos. Sci., 59, 398–413, doi:10.1175/1520-0469(2002)059<0398:Altroa>2.0.Co;2, 2002a.

Torres, O., Decae, R., Veefkind, J. P., and de Leeuw, G.: OMI aerosol retrieval algorithm, in: OMI Algorithm Theoretical Basis Document, NASA Goddard Space Flight Cent., Greenbelt, Md., USA, 47–71, 2002b.

Torres, O., Bhartia, P. K., Sinyuk, A., Welton, E. J., and Holben, B.: Total Ozone Mapping Spectrometer measurements of aerosol absorption from space: comparison to SAFARI 2000 ground-based observations, J. Geophys. Res.-Atmos., 110, D10S18, doi:10.1029/2004JD004611, 2005.

Torres, O., Tanskanen, A., Veihelmann, B., Ahn, C., Braak, R., Bhartia, P. K., Veefkind, P., and Levelt, P.: Aerosols and surface UV products from Ozone monitoring instrument observations: an overview, J. Geophys. Res.-Atmos., 112, D24S47, doi:10.1029/2007jd008809, 2007.

Torres, O., Ahn, C., and Chen, Z.: Improvements to the OMI near-UV aerosol algorithm using A-train CALIOP and AIRS observations, Atmos. Meas. Tech., 6, 3257–3270, doi:10.5194/amt-6-3257-2013, 2013.

Twomey, S.: On the numerical solution of Fredholm integral equations of the first kind by the inversion of the linear system produced by quadrature, J. Assoc. Comput. Mach., 10, 97–101, 1963.

Veihelmann, B., Levelt, P. F., Stammes, P., and Veefkind, J. P.: Simulation study of the aerosol information content in OMI spectral reflectance measurements, Atmos. Chem. Phys., 7, 3115–3127, doi:10.5194/acp-7-3115-2007, 2007.

Wagner, S. C., Govaerts, Y. M., and Lattanzio, A.: Joint retrieval of surface reflectance and aerosol optical depth from MSG/SEVIRI observations with an optimal estimation approach: 2. Implementation and evaluation, J. Geophys. Res.-Atmos., 115, D02204, doi:10.1029/2009jd011780, 2010.

Wurl, D., Grainger, R. G., McDonald, A. J., and Deshler, T.: Optimal estimation retrieval of aerosol microphysical properties from SAGE II satellite observations in the volcanically unperturbed lower stratosphere, Atmos. Chem. Phys., 10, 4295–4317, doi:10.5194/acp-10-4295-2010, 2010.

Young, S. A., Vaughan, M. A., Kuehn, R. E., and Winker, D. M.: The retrieval of profiles of particulate extinction from cloud-aerosol lidar and infrared pathfinder satellite observations (CALIPSO) data: uncertainty and error sensitivity analyses, J. Atmos. Ocean. Tech., 30, 395–428, doi:10.1175/Jtech-D-12-00046.1, 2013.

**Table 1.** Positions and mean AOT and SSA at 388 nm of the AERONET sites during the DRAGON-NE Asia 2012 campaign.

| Site name | Latitude (°) (North) | Longitude (°) (East) | Mean 380 nm AOT | Mean 440 nm SSA |
|---|---|---|---|---|
| Baengnyeong | 37.97 | 124.63 | 0.56 | 0.96 |
| Yonsei Univ., Seoul | 37.56 | 126.94 | 0.63 | 0.93 |
| Anmyeon | 36.54 | 126.33 | 0.57 | 0.94 |
| Bokjeong, Seoul | 37.46 | 127.13 | 0.75 | 0.90 |
| Gangneung Wonju National Univ. | 37.77 | 128.87 | 0.53 | 0.92 |
| Guwol, Seoul | 37.45 | 126.72 | 0.69 | 0.94 |
| GIST, Gwangju | 35.23 | 126.84 | 0.54 | 0.93 |
| HUFS, Yongin | 37.34 | 127.27 | 0.63 | 0.90 |
| Kongju National Univ., Kongju | 36.47 | 127.14 | 0.62 | 0.96 |
| Konkuk Univ., Seoul | 37.54 | 127.08 | 0.67 | 0.92 |
| Korea Univ., Seoul | 37.59 | 127.03 | 0.73 | 0.92 |
| Kunsan National Univ., Kunsan | 35.94 | 126.68 | 0.61 | 0.92 |
| Kyungil Univ., Kyungsan | 36.07 | 128.82 | 0.57 | 0.93 |
| Mokpo National Univ., Mokpo | 34.91 | 126.44 | 0.58 | 0.93 |
| NIER, Incheon | 37.57 | 126.64 | 0.62 | 0.93 |
| Pusan National Univ., Pusan | 35.24 | 129.08 | 0.62 | 0.93 |
| Sanggye, Seoul | 37.66 | 127.07 | 0.73 | 0.92 |
| Sinjeong, Seoul | 37.52 | 126.86 | 0.64 | 0.91 |
| Soha, Seoul | 37.45 | 126.89 | 0.69 | 0.91 |
| Gosan, Jeju | 33.29 | 126.16 | 0.62 | 0.96 |
| Seoul National Univ., Seoul | 37.46 | 126.95 | 0.65 | 0.93 |
| Fukuoka | 33.52 | 130.48 | 0.50 | 0.90 |
| Kohriyama | 37.36 | 140.38 | 0.34 | 0.95 |
| Kyoto | 35.03 | 135.78 | 0.47 | 0.94 |
| Matsue | 35.48 | 133.01 | 0.56 | 0.93 |
| Mt. Ikoma | 34.68 | 135.68 | 0.39 | 0.96 |
| Mt. Rokko | 34.76 | 135.23 | 0.41 | 0.95 |
| Nara | 34.69 | 135.83 | 0.48 | 0.94 |
| Nishiharima | 35.03 | 134.34 | 0.42 | 0.95 |
| North Osaka | 34.77 | 135.51 | 0.52 | 0.94 |
| South Osaka | 34.54 | 135.50 | 0.55 | 0.94 |
| Tsukuba | 36.05 | 140.12 | 0.38 | 0.94 |
| Noto | 37.33 | 137.14 | 0.41 | 0.94 |
| Shirahama | 33.69 | 135.36 | 0.41 | 0.96 |
| Chiba University | 35.63 | 140.10 | 0.31 | 0.92 |
| Fukue | 32.75 | 128.68 | 0.78 | 0.92 |





ACPD
15, 16615–16654, 2015

**Table 2.** Aerosol number-size distribution parameters* and real refractive index ($n_r$) for each aerosol type in the OMI near-UV algorithm.

| Aerosol Model | $r_g$ m1 [µm] | $r_g$ m2 [µm] | $\sigma$ m1 [µm] | $\sigma$ m2 [µm] | FMF | $n_r$ | $n_{i,354/388}$ |
|---|---|---|---|---|---|---|---|
| Sulfate | 0.088 | 0.509 | 1.499 | 2.160 | 0.999596 | 1.40 | 1.0 |
| Smoke | 0.080 | 0.705 | 1.492 | 2.075 | 0.999795 | 1.50 | 1.2 |
| Dust | 0.052 | 0.670 | 1.697 | 1.806 | 0.995650 | 1.55 | 1.4 |

* Number-weighted particle size distribution parameters: fine and coarse mode radii ($r_g$ m1 and $r_g$ m2) and variance ($\sigma$ m1 and $\sigma$ m2), number fine mode fraction (FMF).



Discussion Paper | Discussion Paper | Discussion Paper | Discussion Paper |

ACPD
15, 16615–16654, 2015

An online aerosol retrieval algorithm

U. Jeong et al.

**Table 3.** Retrieval approach criteria of OMI near-UV algorithm version 1.5.3.

| Surface Category | UVAI | CO ($10^{18}$ molecules $cm^{-2}$) | Surface Type | Aerosol Type | Retrieval Approach |
|---|---|---|---|---|---|
| Ocean | $\geq 0.5$ | $> 2.2$ NH (1.8 SH) | NA* | Smoke | Two-channel |
| Ocean | $\geq 0.5$ | $\leq 2.2$ NH (1.8 SH) | NA | Dust | Two-channel |
| Ocean | $< 0.5$ | – | – | – | No retrieval |
| Land | $\geq 0.5$ | $> 2.2$ NH (1.8 SH) | All | Smoke | Two-channel |
| Land | $\geq 0.5$ | $\leq 2.2$ NH (1.8 SH) | All | Dust | Two-channel |
| Land | $< 0.5$ | $> 2.2$ NH (1.8 SH) | All | Sulfate | Two-channel |
| Land | $< 0.5$ | $\leq 2.2$ NH (1.8 SH) | All but arid | Sulfate | Single Channel |
| Land | $< 0.5$ | $\leq 2.2$ NH (1.8 SH) | arid | Dust | Single Channel |

* Not available



Discussion Paper | Discussion Paper | Discussion Paper | Discussion Paper |
ACPD
15, 16615–16654, 2015

An online aerosol retrieval algorithm

U. Jeong et al.

ACPD
15, 16615–16654, 2015

An online aerosol retrieval algorithm

U. Jeong et al.





**Table 4.** Diagonal and off-diagonal elements of the measurement error covariance matrices using two different measurement matrices.

| Measurement matrix | $[I_{354} I_{388}]^{\mathrm{T}}$ | $\left[I_{354} \frac{I_{354}}{I_{388}}\right]^{\mathrm{T}}$ |
|---|---|---|
| First diagonal term | $\sigma(\epsilon_{354})$ | $\sigma(\epsilon_{388})$ |
| Second diagonal term | $\sigma(\epsilon_{388})$ | $\left(\frac{I_{354}}{I_{388}}\right)^2 \left\{\left(\frac{\epsilon_{\mathrm{r},354}}{I_{354}}\right)^2 + \left(\frac{\epsilon_{\mathrm{r},388}}{I_{388}}\right)^2\right\}$ |
| Off-diagonal term | $\sigma(\epsilon_{354}, \epsilon_{388})$ | 0 |

**Table 5.** Error sources and their assumed magnitudes in the OMI ATBD (Algorithm Theoretical Basis Documents) and this study.

| Error source | Error perturbation (OMI ATBD) | Assumed value of $\sigma$ for each error source in this study |
|---|---|---|
| Cloud Contamination | 5 % cloud contamination | NA[b] |
| Surface Reflectivity | 0.01 error in surface reflectivity | 0.01 for both wavelengths |
| Radiometric uncertainty | SNR less than 1 %<br>Radiometric offset additive error of 1 %<br>Radiometric scale factor multiplicative error of 1 % | 2 % of BSDF calibration uncertainty (Dobber et al., 2006)<br>Radiometric precision provided by Level 1b data |
| Size distribution (mode radius) | 5 % increase of mode radius | 0.019 for fine mode[a]<br>0.510 for coarse mode[a] |
| Size distribution (width) | 5 % increase of width | 0.265 for fine mode[a]<br>0.307 for coarse mode[a] |
| Fine mode fraction | NA | 0.0015[a] |
| Refractive index | Increase with 0.05 for $n_r$<br>Increase with 0.01 for $n_i$ | 0.053 for $n_r$ (for all wavelengths and size modes)[a]<br>0.0047 for 354 nm $n_i$[a] |
| Aerosol Vertical Profile | Change of 1 km peak height | Change of 2 km peak height<br>Change of 1 km half width |
| Particle shape | NA | NA |

[a] Standard deviation of each parameter during the DRAGON-NE Asia 2012 campaign. The parameters for $n_r$ and $n_i$ were obtained from 440 nm AERONET inversion products.

[b] Not analyzed.





ACPD
15, 16615–16654, 2015

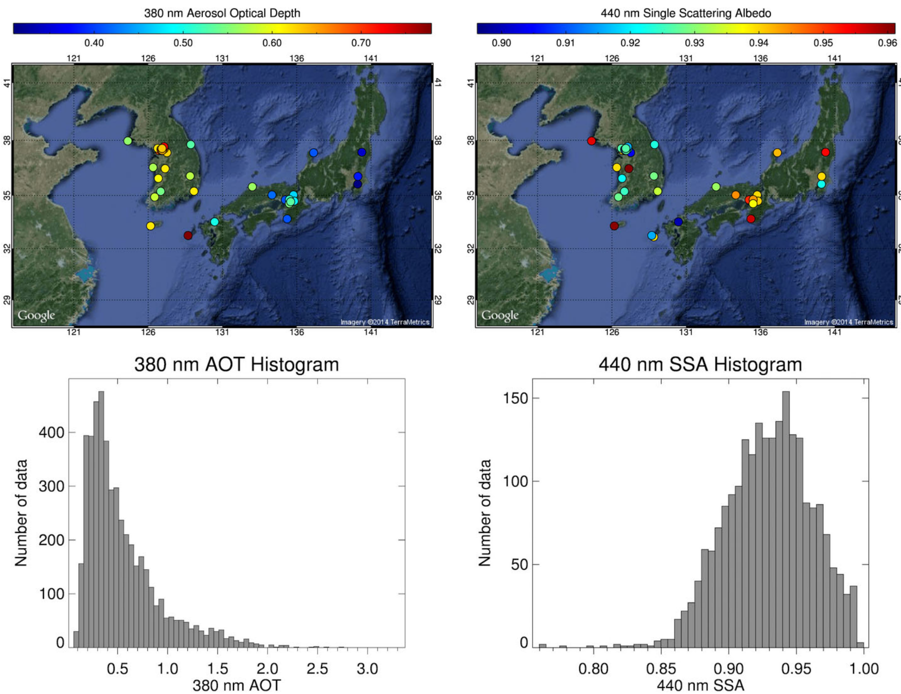


**Figure 1.** Mean 380 nm aerosol optical thickness (AOT) and 440 nm single scattering albedo and their probability density functions during the DRAGON-NE Asia 2012 campaign.





ACPD
15, 16615–16654, 2015

An online aerosol retrieval algorithm

U. Jeong et al.

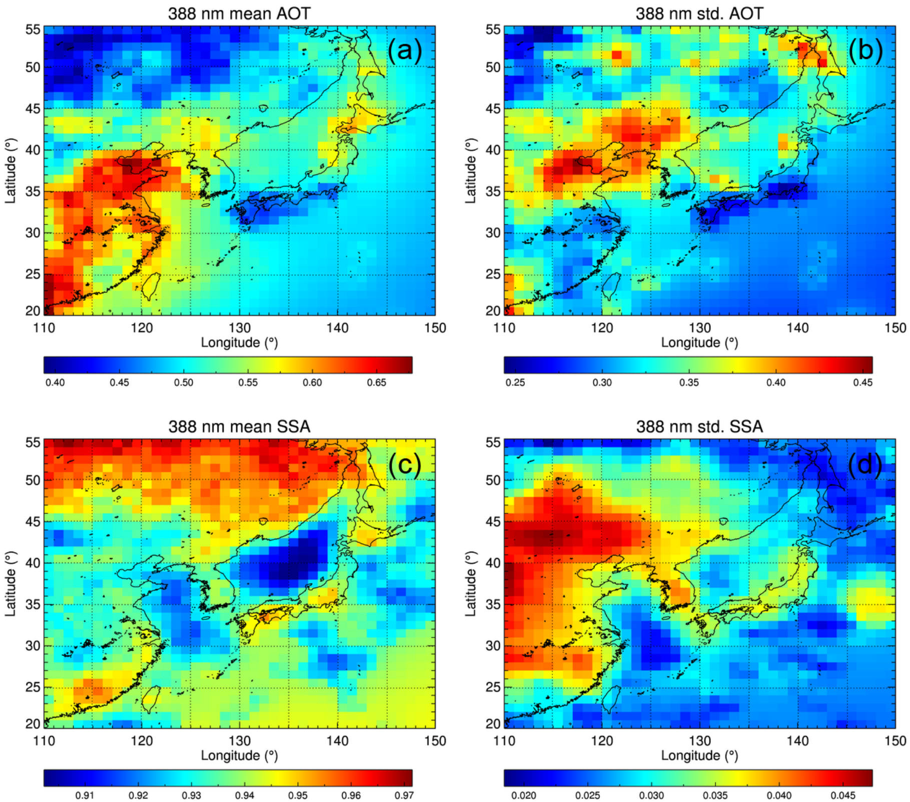


**Figure 2. (a)** Mean and **(b)** standard deviation of 388 nm AOT from the OMAERUV product in spring (March to May) 2005–2014. Panels **(c)** and **(d)** show the average and standard deviation of SSA, respectively, during the same period.





ACPD
15, 16615–16654, 2015

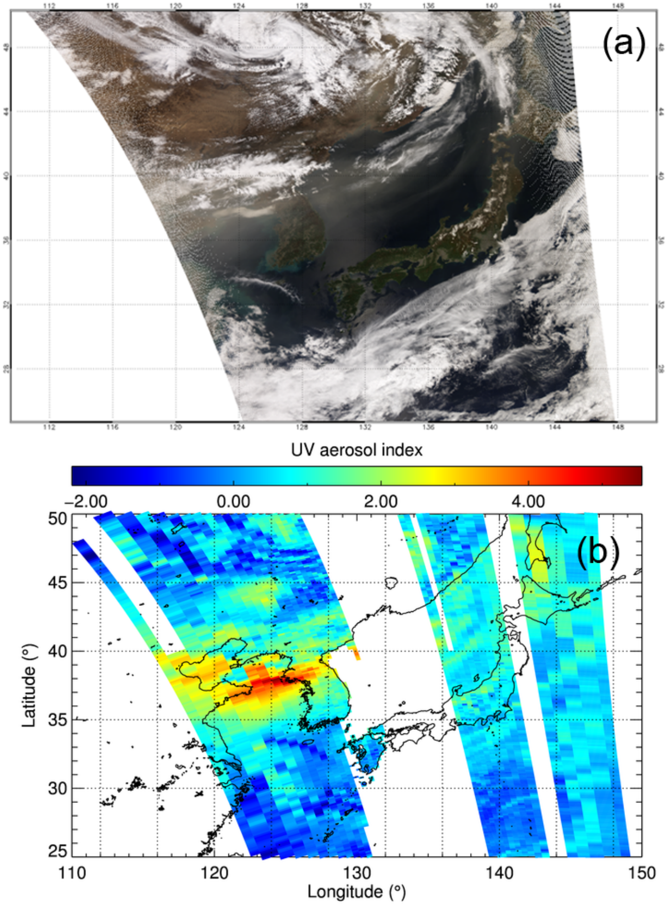


**Figure 3.** **(a)** MODIS Aqua true color image and **(b)** UV aerosol index from the OMI product in Northeast Asia on 28 April 2012.





ACPD
15, 16615–16654, 2015

An online aerosol retrieval algorithm

U. Jeong et al.

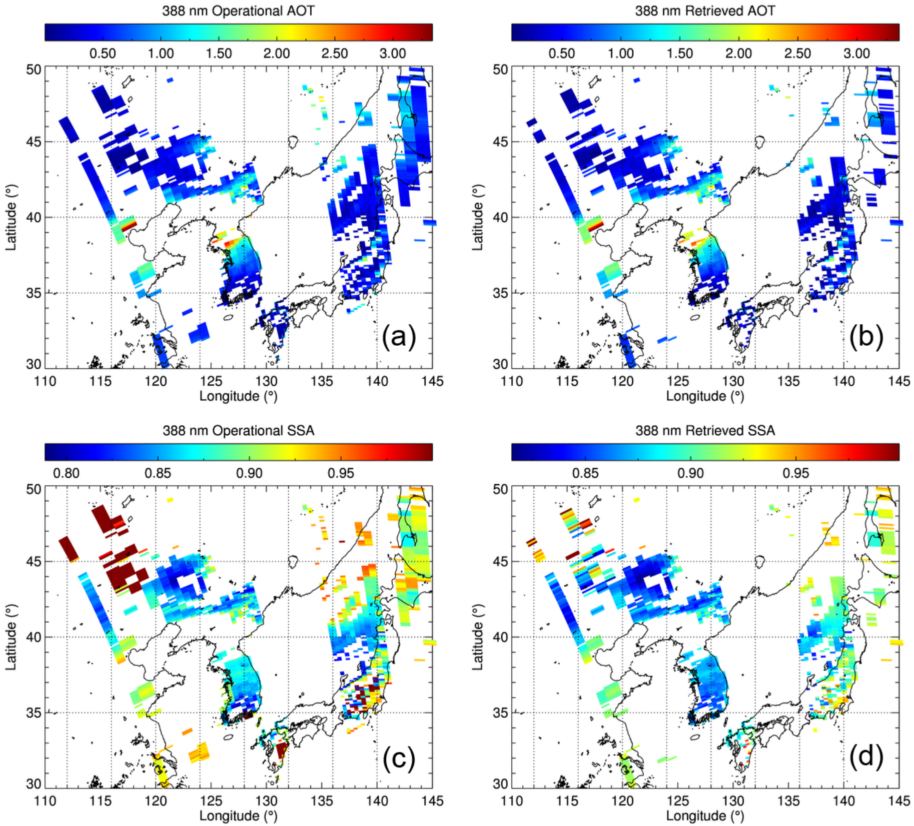


**Figure 4. (a)** OMI operational AOT, **(b)** OE-based AOT, **(c)** operational SSA, and **(d)** OE-based SSA on 28 April 2012 at 388 nm.





ACPD
15, 16615–16654, 2015

An online aerosol retrieval algorithm

U. Jeong et al.

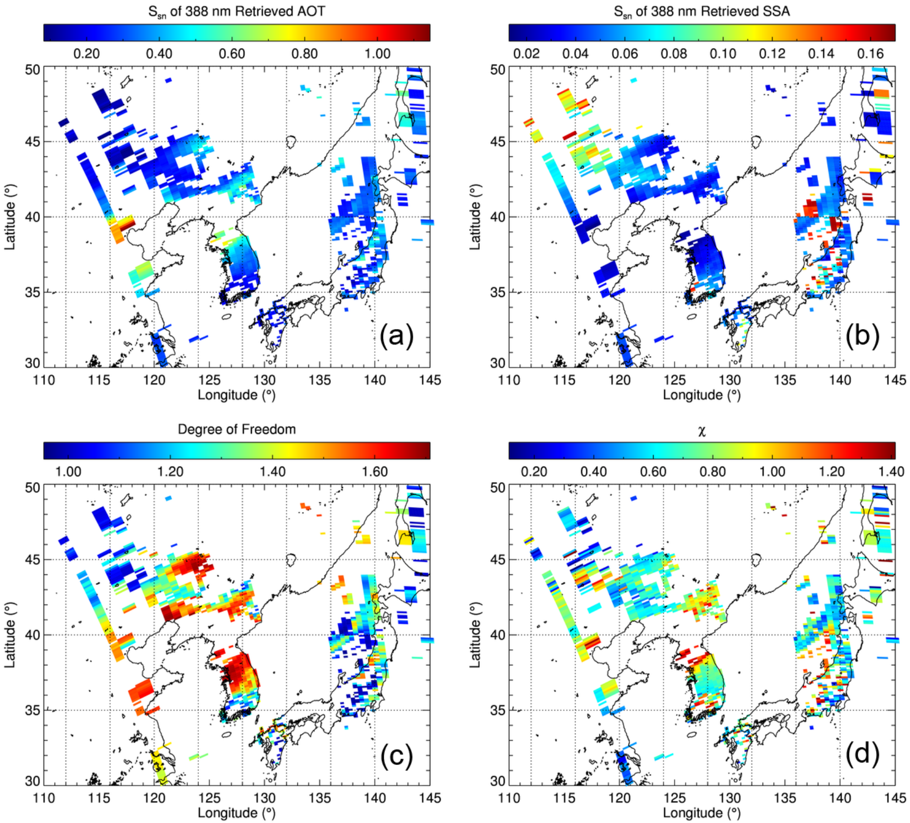


**Figure 5.** Estimated $\mathbf{S}_{sn}$ of **(a)** OE-based 388 nm AOT and **(b)** SSA. Panels **(c)** and **(d)** show the degrees of freedom and cost function of the retrieval, respectively.





ACPD
15, 16615–16654, 2015

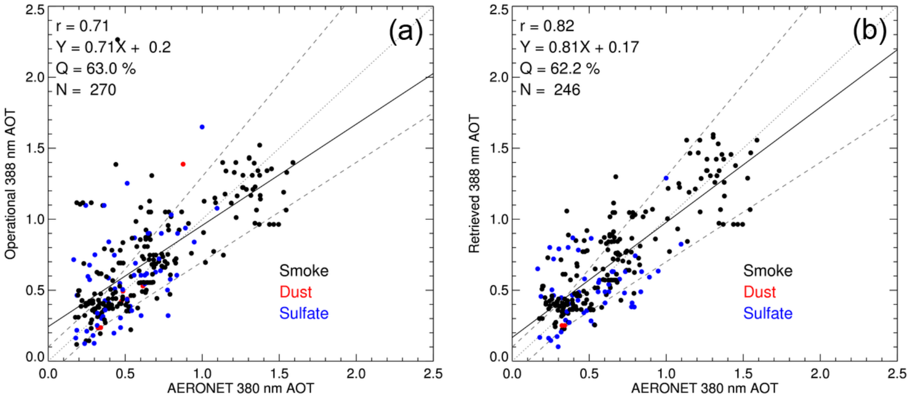


**Figure 6.** Validation of 388 nm AOT against AERONET data from **(a)** operational products and **(b)** the OE-based algorithm during the DRAGON-NE Asia 2012 campaign.





ACPD
15, 16615–16654, 2015

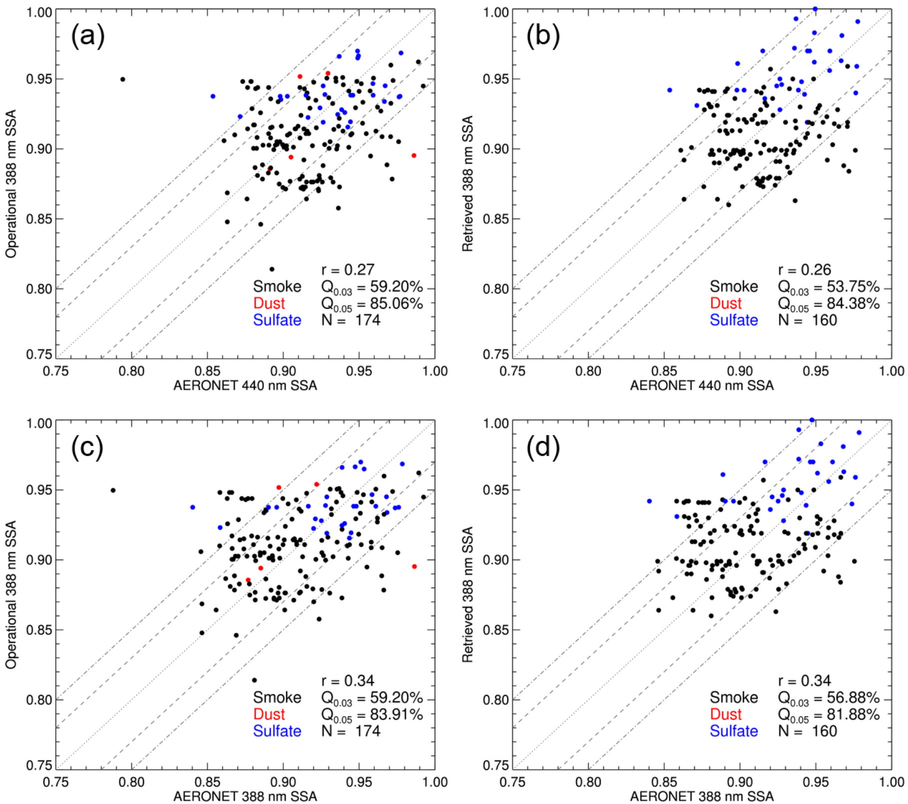


**Figure 7.** Comparison of the 440 nm SSA from AERONET and 388 nm SSA from **(a)** the operational products and **(b)** the OE-based algorithm, during the DRAGON-NE Asia 2012 campaign. Panels **(c)** and **(d)** compare converted 388 nm SSA from AERONET with that from **(c)** the operational products and **(d)** the OE-based algorithm.





ACPD
15, 16615–16654, 2015

An online aerosol retrieval algorithm

U. Jeong et al.

Title Page
Abstract Introduction
Conclusions References
Tables Figures
◀◀ ▶▶
◀ ▶
Back Close
Full Screen / Esc
Printer-friendly Version
Interactive Discussion

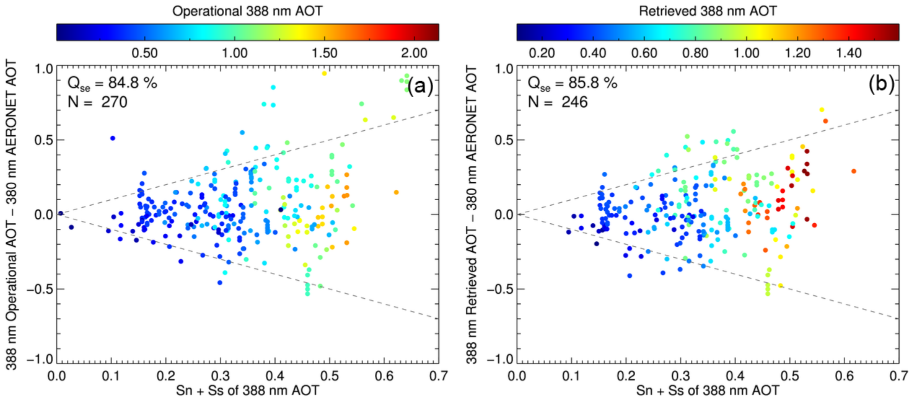


**Figure 8.** Comparison between estimated uncertainties of the 388 nm AOT from the OE-based algorithm ($x$ axis) and biases of **(a)** operational AOT and **(b)** OE-based AOT from AERONET measurements ($y$ axis).





ACPD
15, 16615–16654, 2015

An online aerosol retrieval algorithm

U. Jeong et al.

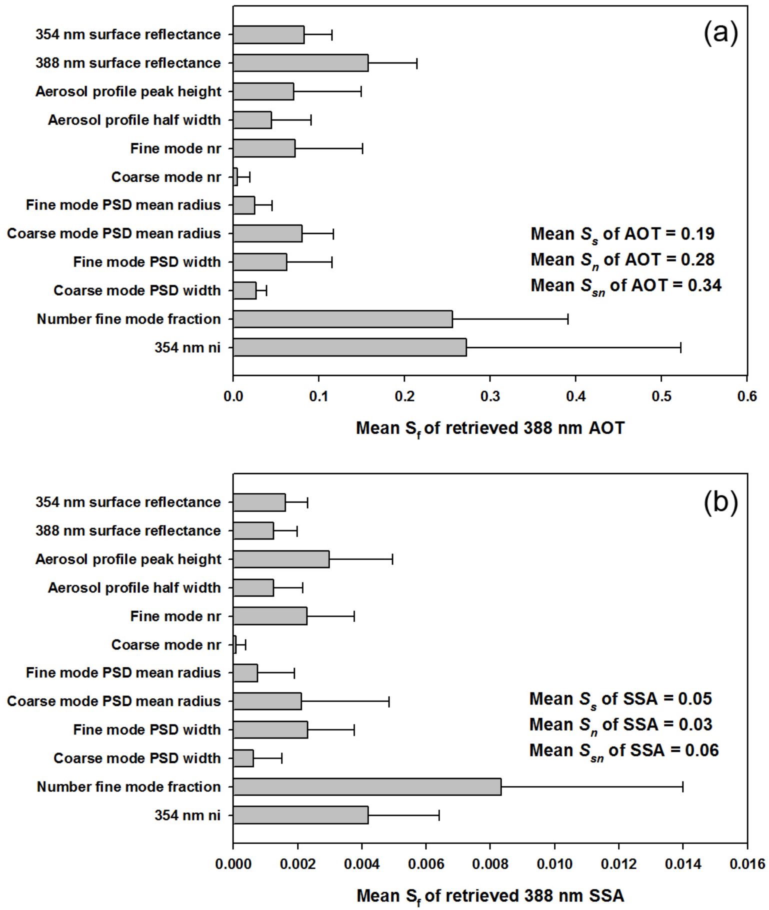


**Figure 9.** Average (gray bars) and standard deviation (black lines) of the forward model parameter errors of 388 nm **(a)** AOT and **(b)** SSA.





ACPD
15, 16615–16654, 2015